Finite-Length, Large-Amplitude Diocotron Mode Dynamics

N. C. Hurst, J. R. Danielson, C. J. Baker and C. M. Surko

9500 Gilman Drive, Physics Department, University of California, San Diego, La Jolla CA 92093

Abstract. The $m = 1$ diocotron mode is an important feature of the dynamics of single-component plasmas confined in Penning-Malmberg traps. Presented here are calculations of the diocotron mode frequency under conditions where the most commonly used approximations are invalid. One important application of the calculation described here is the operation of a multi-cell Penning-Malmberg trap that employs a low-aspect-ratio “master" cell. Measurements of the mode frequency in a prototype device are presented. The predictions of the calculation are in good agreement with the data, even for mode amplitudes approaching the inner radius of the electrodes.

Keywords: Non-neutral plasma, diocotron mode, Penning-Malmberg trap, space-charge potential
PACS: 52.27.Jt, 52.35.Mw, 52.35.Fp

INTRODUCTION

Single-component plasmas (SCP) confined in Penning-Malmberg traps have been, and continue to be, the subject of extensive study, driven in large part by a wide range of applications [1]. These SCPs are useful in many research areas including particle, atomic, plasma, and condensed matter physics; fluid dynamics, and material science. Single-component plasmas are used to trap and cool antiparticles [2], and to subsequently generate antiparticle beams [3, 4, 5, 6]. Such beams are used in a variety of applications including studies of binding and annihilation of positrons with molecules [7], scattering experiments [8], the production of antihydrogen [9], the creation of electron-positron plasmas [10], efforts to create positronium Bose-Einstein condensates [11], and the study of materials [12, 13]. Additionally, SCPs exhibit many interesting phenomena from the perspective of basic plasma science, including the relaxation to thermal equilibria [14] and the ability to achieve infinite plasma confinement times [15].

Some of these applications either require, or benefit from, the availability of large numbers of trapped antiparticles. To this end, research is being conducted with the goal of building a high-capacity positron trap. Progress in this effort has necessitated the design and construction of a novel type of particle trap - a high magnetic field multi-cell Penning-Malmberg (PM) trap, in which separate SCPs are stored in parallel in a bank of compact traps that share a common vacuum and superconducting magnet system [16].

Experiments addressing the basic plasma physics of multi-cell trap (MCT) operation have resulted in a number of interesting discoveries. When a magnetized SCP is displaced from the axis of symmetry in a PM trap, the plasma executes a circular orbit about the trap axis (the so-called "diocotron mode") which is due to the $\mathbf{E} \times \mathbf{B}$ motion of the plasma arising from the image-charge electric fields. It was found that, when a SCP simultaneously spans both a large-diameter master cell and an off-axis storage cell in a MCT, it executes non-circular diocotron-like orbits about a stationary point, with the motion characterized by the competition of the bounce-averaged diocotron drifts in the two cells [17]. It was also observed that, during autoresonant excitation of the diocotron mode [18] to high amplitude, the plasma can eventually lose phase lock and sometimes suffer partial or total destruction (i.e. particle loss to the wall) [19].

Plasmas have now been trapped in the off-axis storage cells of a MCT. Details of this and other related phenomena, such as high-space-charge plasma confinement and inter-cell plasma transfer dynamics, will be covered in a future publication [20]. Quantitative understanding of the diocotron mode frequency has proven to be essential to the development of a predictive model of the plasma dynamics in the low-aspect-ratio master cell. Improved calculations are presented here for the mode frequency as a function of plasma displacement D and total particle number N for a wide range of both parameters, under only one assumption, namely that the plasma radius is much smaller than the wall radius.

Non-Neutral Plasma Physics IX
AIP Conf. Proc. 1668, 020003-1–020003-9; doi: 10.1063/1.4923106

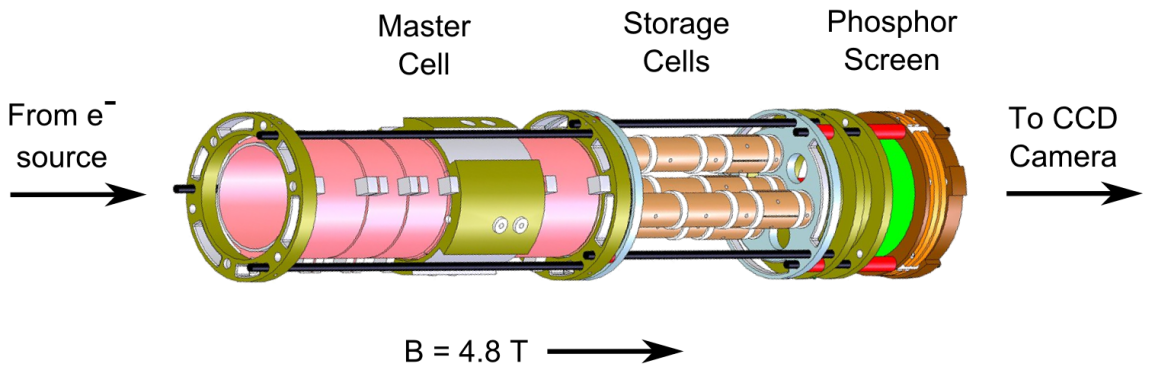

FIGURE 1. Arrangement of multi-cell test structure (MCTS).

DESCRIPTION OF THE EXPERIMENTS

The apparatus used for these experiments is a prototype of a multi-cell Penning-Malmberg trap, dubbed the Multi-Cell Test Structure (MCTS) that has been in operation recently at U. C. San Diego. The goal is to design traps to store ever larger numbers of positrons. A principle impediment to this is that the plasma space charge potential Φ_p developed at large N/L_p, where N is the total particle number and L_p is the plasma length, can become too large for practical axial confinement potentials Φ_c. The MCT employs multiple storage cells in parallel, using metal electrodes to shield separate plasmas from each other. Since plasma potential $\Phi_p \propto N/L_p$, arranging x plasmas in parallel reduces the required potential Φ_c by a factor of x for a given N.

The MCTS is illustrated in Fig. 1. It consists of three axial sections: a large-diameter “master" cell, a bank of 4 smaller storage cells, and a phosphor screen assembly for imaging the plasmas, all of which are immersed in a 4.8 T magnetic field. The master cell has a wall radius $R_w = 3.8$ cm and a trap length $L_t = 15.5$ cm. Of the four storage cells, one shares a common axis with the master cell and has $R_w = 0.8$ cm, while the other three are located 3 cm off of the axis of symmetery and have wall radii 0.8, 0.6, 0.4 cm. All storage cells have trap lengths of 15 cm. All cells, including the master, have one electrode spanning a fraction of the trap length which is divided into four equal 90° segments that can be independently biased. These segmented electrodes are used for so-called rotating wall (RW) plasma compression, autoresonant diocotron-mode amplitude control, and as a plasma diagnostic.

Experiments in the MCTS, thus far, operate with electron plasmas for increased data rate. The master cell is filled on axis with electrons using a heated-cathode electron gun located in a region of lower field. It generates ~ 100 nA in circular area corresponding to about 0.25 mm in radius in the 4.8 T field. Filling off-axis storage cells is accomplished by first transporting the plasma across the magnetic field using autoresonant diocotron excitation, and then transferring plasma axially into a storage cell. The plasma is diagnosed by grounding one of the confinement electrodes and accelerating electrons through + 5 kV to then allow them to impinge on the phosphor screen. The resulting light is imaged with the CCD camera with a resolution of about $(55\ \mu\text{m})^2$ / pixel and a noise floor of roughly 3000 e^- / pixel. Note that plasmas trapped in the master cell can only be imaged by passing through the storage cells, thus restricting the range of plasma displacements D that can be imaged. An additional diagnostic tool is the pick up signal on one of the 90° sectors of the segmented electrodes.

Typical characteristics of the plasmas in the master (storage) cell are as follows: The total electron number N can vary up to roughly 10^9, limited by the space charge potential Φ_p, which ranges up to 80 (95) V. Plasma lengths are $L_p \leq 20$ (≤ 17) cm, densities are typically $n \sim 1-2\times 10^8$ cm^3, RMS plasma radii occupy the range $0.25-2$ mm, and plasma temperatures are $T \sim 0.1$ eV. The $m = 1$ diocotron mode frequency ranges up to 1 (5) kHz, typical $\mathbf{E}\times\mathbf{B}$ rotation frequencies are 30-60 kHz, and axial bounce frequencies are 1 - 10 MHz.

THE DIOCOTRON MODE FOR SINGLE-COMPONENT PLASMAS IN PENNING-MALMBERG TRAPS

The diocotron mode in a PM trap is the $\mathbf{E}\times\mathbf{B}$ drift orbit of the plasma due to the electric field from the image charge induced at the surfaces of the confining electrodes. It has been studied extensively for the case of pure electron plasmas. Focus here is restricted to the case of azimuthal wavenumber $m = 1$. For axial particle bounce times much smaller than the perpendicular drift timescale, this mode represents a circular trajectory of a rigid-rod plasma in the (r,θ) plane about the symmetry axis. Note that the electron plasma column also experiences an $\mathbf{E}\times\mathbf{B}$ rigid rotation about its axis due to the self field. However, for the conditions studied here, the timescale for this motion is fast compared to, and has no significant effect on, the diocotron drift motion. Predictions for the diocotron mode frequency have been obtained under a variety of assumptions, many of which are invalid in the MCTS due to design constraints on trap architecture in the context of the goal of developing a high-capacity trap. Presented here is a brief overview of previous work on the subject, followed by description of a new model and experimental tests of diocotron mode frequencies in the MCTS master cell.

The most basic analysis of the diocotron mode in a PM trap involves considering a line of charge, infinite in axial extent and infinitesimal in radial extent [21]. The motion is in two dimensions (r,θ) and $R_p \to 0$ where R_p is radius of the plasma column. The $\mathbf{E}\times\mathbf{B}$ drift velocity is calculated from the electric field from the image line charge located at $r_i = R_w^2/D$, where D, the amplitude of the mode, is the displacement of the plasma from the axis of symmetry. The linearized infinite-length diocotron frequency for $D/R_w \ll 1$ and the full nonlinear formula are given (respectively) by

$$f_1 = \frac{cNe}{\pi L_p B R_w^2}, \tag{1}$$

and

$$f_\infty = f_1\left[\frac{1}{1-(D/R_w)^2}\right]. \tag{2}$$

The next level of analysis involves consideration of the finite radius of the plasma column. Physically, the normally circular areal density profile of the plasma $\langle n\rangle_z(r,\theta) \equiv (1/L_p)\int dz\, n(r,\theta,z)$ becomes distorted as it approaches the wall (i.e. as $D/R_w \to 1$). This problem has been solved to order $(D/R_w)^2$ by considering the quadrupole perturbation of the plasma profile [22]. The resulting formula for the diocotron drift frequency f_q, now valid for finite plasma radius R_p, is

$$f_q = f_1\left[1+\frac{1-2(R_p/R_w)^2}{[1-(R_p/R_w)^2]^2}\left(\frac{D}{R_w}\right)^2\right]. \tag{3}$$

The previous analysis assumes a uniform elliptic patch of constant areal electron density. Another analysis considers more general plasma profiles [23], the result being a fairly complicated expression that is not particularly relevant here.

Finally, one may call into question the assumption that the plasma is infinite in axial extent. In this case, two factors contribute to the diocotron frequency shift: the finite extent of the image charge, and the force on the plasma ends due to the electric fields from the axial confinement potentials of the PM trap. The former contribution f_i, due to finite length of the image charge, must be considered when the assumption $R_w/L_p \ll 1$ breaks down. The latter contribution f_c, due to axial confinement fields, must be considered when the assumption $|\Phi_p|/|V_c| \ll 1$ is invalid. The latter contribution to the frequency is related to the "magnetron" drift effect experienced by single particles in a PM trap.

These finite length effects can be thought of as corrections, or "shifts" to the infinite length formula. The image field contribution is reduced by some amount $\Delta f_i < 0$, and the confinement field produces a contribution $f_c > 0$. This problem has been solved to lowest order in D/R_w, R_p/R_w, R_w/L_p, and $|\Phi_p|/|V_c|$ by Fine & Driscoll [24], a calculation referred to here as "FD98". The diocotron frequency shifts calculated in FD98 are

$$\Delta f_i = -0.671 f_1\left(\frac{R_w}{L_p}\right) \tag{4}$$

$$f_c = f_1\frac{j_{01}}{2}\left(\frac{1}{4}+\log\frac{R_w}{R_p}+\frac{TL_p}{Ne^2}\right)\left(\frac{R_w}{L_p}\right) \tag{5}$$

where $j_{01} = 2.405$ is the first zero of the J_0 Bessel function.

The multi-cell trap application discussed here imposes specific constraints on what assumptions can be made in the construction of a model for the diocotron frequency. An expansion in D/R_w will not work. The model must be valid for the full range $0 \leq D/R_w < 1$, since the plasma reaches $D/R_w = 0.8$ for the off-axis transfers into the storage cells of the MCTS. Due to the small aspect ratio of the master cell, it is also not appropriate to make the approximation $R_w/L_p \ll 1$. Finally, in order to maximize N, the trap must be operated in a high-space-charge regime, where the plasma potential is on the order of axial containment potential, $|\Phi_p| \sim |V_c|$, a regime that has not previously been studied to any great extent.

The effect of plasma temperature can be neglected, except for small N, $\leq 10^7$ e^-, on the grounds that $\Phi_p/T \gg 1$ due to strong cyclotron cooling. The effect of finite plasma radius can also be neglected based on the fact that typically $R_p/R_w < 0.1$. Further, even at $D/R_w = 0.8$ the plasma profiles appear circular, indicating that quadrupole perturbations are unimportant in calculating the image-charge electric fields. As described below, the two frequency contributions are calculated separately, and then their sum $f_d = f_c + f_i$ is compared with experimental data and the predictions of FD98.

THE CONFINEMENT FIELD CORRECTION

Laplace's equation is solved for the azimuthally symmetric vacuum confinement potential Φ_c on the domain $0 \leq z \leq z_\infty$, $0 \leq r \leq R_w$. Here, the end of the cylinder at z_∞ extends past the physical trap region in order to model finite-length confinement electrodes. The faces of the cylinder are chosen to be at ground, and the wall of the cylinder is split into five regions, labeled in Fig. 2, where the potential is specified piece-wise. Region I is grounded, corresponding to the central PM trap electrode, region III is held at potential $-V_c$, corresponding to the PM trap confinement electrode, and region V is grounded (and extends to z_∞). Regions II & IV represent small gaps where the potential increases/decreases linearly between $-V_C$ and ground so as to avoid unphysical infinite electric fields. The value of z_∞ can be chosen almost arbitrarily with little effect on the calculation. The Laplace solution is

$$\Phi_c(r,z) = \sum_{n=1}^{\infty} A_{0n} I_0\left(\pi n r/z_\infty\right) \sin\left(\pi n z/z_\infty\right), \tag{6}$$

where

$$A_{0n} = \left(\pi z_\infty I_0\left(\pi n R_w/z_\infty\right)\right)^{-1} 2\pi \int dz \sin\left(\pi n z/z_\infty\right) \Phi(r = R_w, z), \tag{7}$$

I_0 is the modified Bessel function of the first kind, and $\Phi(r = R_w, z)$ is the specified potential on the wall of the PM trap.

The confinement electric field has both $\hat{\mathbf{r}}$ and $\hat{\mathbf{z}}$ components. $E_{cz} = -\partial_z \Phi_c$ provides axial confinement, while the non-zero value of $E_{cr} = -\partial_r \Phi_c$ gives rise to an $\mathbf{E} \times \mathbf{B}$ drift of the plasma in the azimuthal direction. It adds to the zeroth-order diocotron motion, thus producing a frequency shift. Since E_{cr} varies with z, the forces on the plasma particles vary during the axial bounce motion. In the experiments described here, the axial bounce time is much smaller than the diocotron-drift timescale. Thus this force is bounce-averaged and multiplied by the particle number N to get the total force on the plasma. This is equivalent to calculating the instantaneous force on the entire plasma, since $n(z)$ is assumed constant (which is equivalent to the statement that Debye length is small compared to L_p). Due to the fact that $R_p/R_w \ll 1$, the electric potential is approximately constant across the profile: $|\Phi_p(\rho = 0) - \Phi_p(\rho = R_p)| \ll |\Phi_p(\rho = 0)| \equiv \Phi_p$, where ρ is the radial coordinate centered on the centroid of plasma density.

Under these assumptions, the plasma potential at a given displacement is

$$\Phi_p(D, z = 0) = \lambda \left[1 + 2\ln\left(\frac{1}{R_p}\sqrt{\frac{(D+R_p)^2 D^2}{R_w^2} + R_w^2 - 2D(D+R_p)}\right)\right], \tag{8}$$

where $\lambda \equiv -eN/L_P$ is the charge per unit length of the plasma column. In the limit $D/R_w \to 0$, this expression reproduces the familiar one, $\Phi_P = \lambda(1 + \ln(R_w/R_p))$. Although Eq. 8 presumes a "point" plasma, the plasma radius R_p does enter the expression. Consistent with the experiments described here, R_p is chosen to be 0.5 cm. The results are weakly dependent on this parameter, since it appears only in the logarithm. The resulting radial electric force on the plasma is then given by

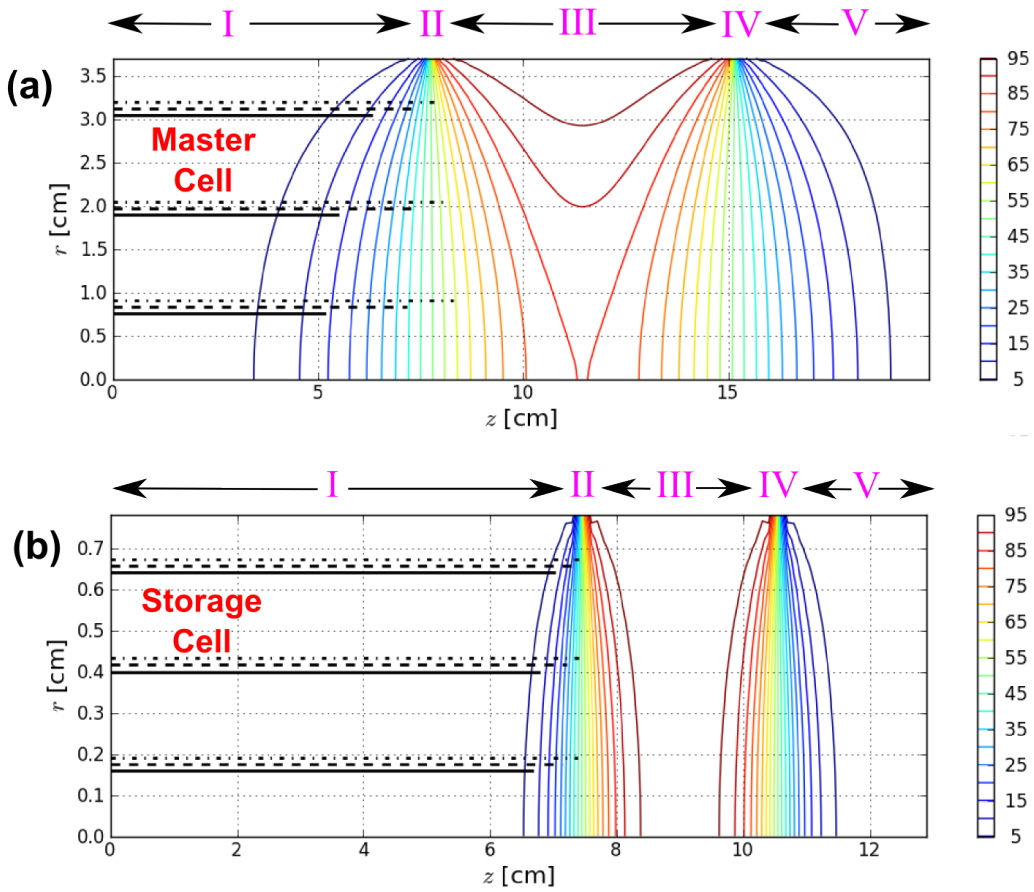

FIGURE 2. Confinement potential contours for the master cell **(a)** and storage cell **(b)**, for the confinement electrodes biased to -100 V. Assuming reflection symmetry about $z = 0$, only half the PM trap is shown. Also shown are the lengths of plasmas with different N at three different displacements: $N = 2 \times 10^8$ (—), 9×10^8 (- - -), 16×10^8 (— · —·).

$$F_{cr} = 2\lambda \int_0^{L_p/2} dz\, E_{cr} = -2\lambda \sum_{n=1}^{\infty} A_{0n} \left[\cos\left(\pi n (L_p/2)/z_\infty\right) - 1 \right] I_1\left(\pi n D/z_\infty\right). \tag{9}$$

Determination of L_p in this expression amounts to equating half of the plasma potential, $\Phi_p/2$ to the confinement potential (given in Eq. 6), which gives the classical turning point

$$|\Phi_p/2 - \Phi_c(r = D, z = L_p/2)| = 0. \tag{10}$$

The factor of 1/2 is a result of the condition that the equilibrium plasma maintains an axial equipotential. This requires that the potential at the turning point be equal to the vacuum potential at that point, and that the sum of the two equal the plasma potential at $z = 0$ (i.e., where it is assumed that the vacuum potential is zero). This transcendental equation for L_p is solved numerically, returning a unique value of L_p for a given particle number N and displacement D/R_w for the specified trap geometry and confinement voltage. Fig. 2 shows the results of this solution, both in the master and storage cell, for different N and D/R_w . Note that for higher N, the space charge pushes the plasma into the confinement electrode (region III), and dL_p/dD switches sign from + to - as Φ_p crosses $V_c/2$. In the high-aspect-ratio storage cell, the length change with D is less drastic, and the plasma potential for a given N is reduced by the logarithmic term.

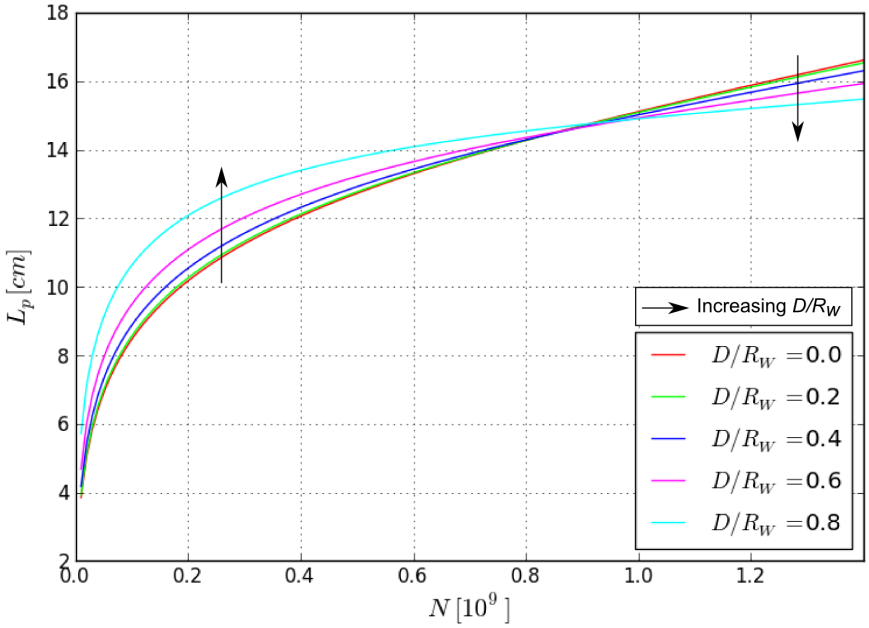

FIGURE 3. Plasma length L_p in the master cell as a function of both total particle number N and displacement D/R_w, as calculated by solving Eq. 10. Arrows indicate sign change of dL_p/dD.

Figure 3 shows plasma length in the master cell as a function of N and D/R_w, calculated from Eq. 10. The sign change of dL_p/dD is evident at $N \sim 9\times10^8\ e^-$.

Given L_p, the confinement-field diocotron mode frequency shift f_c follows directly from Eq. 9. Here, the plasma length is the only parameter lacking for a fully analytic formula for the confinement field frequency shift. Once the radial electric force on the plasma is calculated, f_c follows from the $\mathbf{E}\times\mathbf{B}$ drift velocity, thus

$$f_c = -\frac{cF_{cr}}{2\pi eNBD}. \tag{11}$$

SHIFT DUE TO FINITE-LENGTH OF THE IMAGE CHARGE

The approach used here is to follow the calculation of FD98, but without making assumptions as to the magnitude of D/R_W, L_p/R_w, or $|\Phi_p|/|V_c|$. These approximations allowed FD98 to arrive at an analytical expression for the shift Δf_i; relaxing them means that one must resort to a numerical solution. The calculation involves expressing the electric potential inside the trap due to the finite image charge as an integral over the appropriate Green's function. As before, the drift of the plasma column may be thought of as either the force on a single particle in a bounce-averaged potential or on the entire line-charge at one instant in time. Adopting the former picture, the bounce-averaged electric field is given by

$$\langle E\rangle_b = \frac{1}{L_p}\int_{-L_p/2}^{L_p/2} dz(-\partial_r\phi_i|_{r=D}), \tag{12}$$

where the potential due to the finite-length image charge is

$$\phi_i(r,\theta,z) = \int_{-L_p/2}^{L_p/2} dz' \int dr' \int r' d\theta\lambda\,\delta(\theta')\frac{\delta(r'-D)}{D}G_i(\mathbf{r},\mathbf{r}'), \tag{13}$$

and the Green's function for the image charge is

$$G_i(\mathbf{r},\mathbf{r}') = -\frac{4}{\pi}\int_0^\infty dk\ \cos(k(z-z'))\Big[\frac{1}{2}\frac{K_0(kR_w)}{I_0(kR_w)}I_0(kr_<)I_0(kr_>) + \sum_{m=1}^{\infty}\frac{K_m(kR_w)}{I_m(kR_w)}I_m(kr_<)I_m(kr_>)\cos(m(\theta-\theta'))\Big]. \tag{14}$$

The resulting expression for $\langle E\rangle_b$ is an integral over k which is a function of (L_p/R_w) and (D/R_w), and must be evaluated numerically, using Eq. 10 for the plasma length. This calculation is then inserted into the $\mathbf{E}\times\mathbf{B}$ drift formula to give the image-field portion of the $m=1$ diocotron frequency,

$$f_i = \frac{c}{2\pi DB}\langle E\rangle_b. \tag{15}$$

The frequency shift Δf_i is found by subtracting the infinite length formula Eq. 2 from Eq. 15.

COMPARISON OF THE MODEL AND EXPERIMENT

Comparison of the experimental data with the model predictions for the diocotron frequency as a function of total particle number N is shown in Fig. 4 for plasmas near the axis of the trap (note that space charge potential increases with N). Also shown are the separate contributions to the model predictions from the confinement and image fields, Eqs. 11 and 15 respectively, and the predictions of the FD98 model. The image contribution from FD98 is identical to that of the present work because the $D/R_w \ll 1$ criterion is satisfied; however FD98 overpredicts f_c for higher N because that calculation uses a confinement potential that increases exponentially away from $z=0$ with the assumption $|\Phi_p| \ll |V_c|$. A similar comparison was carried out for the high-aspect-ratio storage cell; and as expected, the present model agrees well with experimental data and converges to the FD98 result (for smaller values of N).

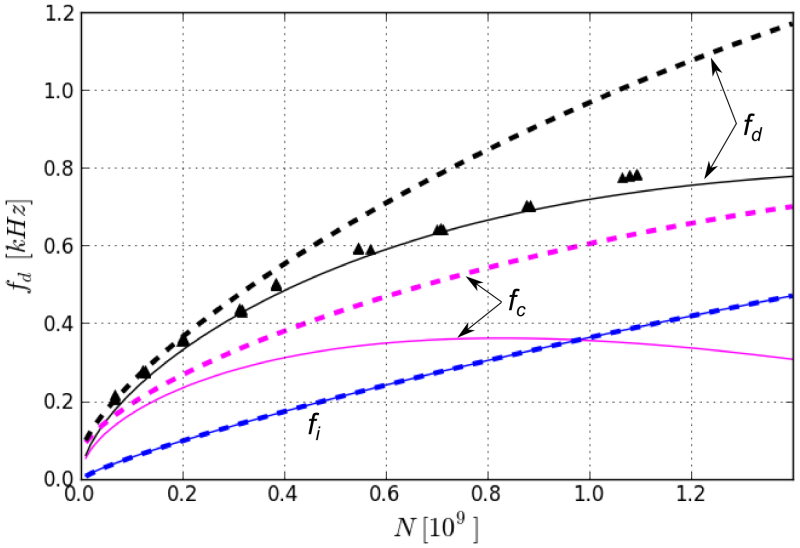

FIGURE 4. Diocotron frequency f_d as a function of total particle number N for plasmas near the axis in the master cell. Data (black triangles) are compared with the FD98 model (- - -) and the present work (—). The separate contributions from confinement fields f_c (—) and from image fields f_i (—) are also shown, with the black lines showing the sum $f_d \equiv f_c + f_i$.

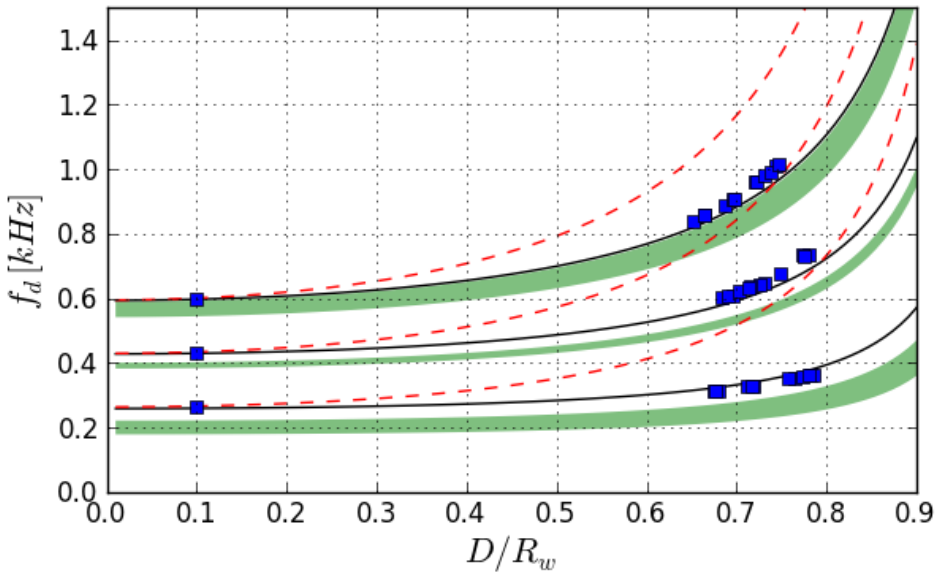

FIGURE 5. The diocotron frequency f_d in the master cell is shown as a function of the displacement D/R_W for three values of N. Green shaded regions represent predictions of the present model including variations of the N values for the data. Solid black lines are predictions of the model, with N chosen to fit the on-axis linear frequency. Dashed lines show the predictions of Eq. 2, normalized to fit the on-axis linear frequency.

Fig. 5 shows diocotron frequency data as a function of D/R_w for three different total particle numbers, $N \approx 0.8$, 2.4, 4.7 $\times 10^8$ e^-, and compares them with the present model as well as that of Eq. 2. The model and data are in good agreement, while the infinite-length formula fails at large D/R_w. The drift due to the confinement field drops as the plasma moves radially outward, because the vacuum electric field has a smaller radial component near the wall. In addition, N/L_p decreases as the plasma lengthens at high D/R_W (i.e., for $\Phi_p < V_c/2$, which is the case for these data). Both of these effects reduce the diocotron frequency relative to the prediction of Eq. 2.

SUMMARY

A detailed understanding of diocotron mode dynamics is necessary in some applications such as the successful operation of a multi-cell trap. Previous calculations of the diocotron mode frequency fail to reproduce the behavior observed in a realistic MCT architecture due to the nature of the approximations made. The calculations of finite-length effects presented here show much improved agreement with experimental data from a prototype MCT, to the extent that this approach will be of considerable value in developing practical MCT systems. More generally, the approach described here can be expected to be useful for any low-aspect ratio PM operating with either high space charge or a large amplitude $m = 1$ diocotron mode. For example, applications with spatial constraints may benefit from short, low aspect ratio traps, in which case the model presented here would be appropriate.

ACKNOWLEDGMENTS

The authors wish to thank E. A. Jerzewski for expert technical assistance and the U. S. Defense Threat Reduction Agency (DTRA) for supporting construction and operation of the MCTS apparatus.

REFERENCES

1. T. M. O'Neil, *Physics Today* **52**, 2, 24 (1999).
2. R. G. Greaves, M. D. Tinkle, C. M. Surko, "Experiments with trapped positron plasmas", edited by J. Fajans and D. H. E. Dubin, AIP Conf. Proc. No 331 (AIP, New York, 1995), pp. 70–86.
3. M. R. Natisin, N. C. Hurst, J. R. Danielson, C. M. Surko, "Recent Progress in Tailoring Trap-based Positron Beams", AIP Conf. Proc. 1521, AIP Press, Melville NY, 2013, pp. 154–164.
4. T. R. Weber, J. R. Danielson, C. M. Surko, *Phys. Plasmas* **15**, 012106 (2008).
5. T. R. Weber, J. R. Danielson, C. M. Surko, *Phys. Plasmas* **16**, 057105 (2009).
6. T. R. Weber, J. R. Danielson, C. M. Surko, *Phys. Plasmas* **17**, 123507 (2010).
7. A. C. L. Jones, J. R. Danielson, M. R. Natisin, C. M. Surko, *Phys. Rev. Lett.* **110**, 223201 (2013).
8. J. P. Marler, "New Results for Positron Scattering from Noble Gas Atoms and Diatomic Molecules", Ph.D. thesis, University of California - San Diego, 2005 (unpublished).
9. C. Amole, et. al., *Phys. Plasmas* **20**, 043510, (2013).
10. T. S. Pedersen, et. al., *New J. Phys.* **14**, 035010, (2012).
11. D. B. Cassidy and A. P. Mills, *Nature* **449**, 195 (2007).
12. P. J. Schultz, K. G. Lynn, *Rev. Mod. Phys.* **60**, 701 (1988).
13. D. W. Gidley, H. G. Peng, R. S. Vallery, *Annu. Rev. Mater. Res.* **36**, 49 (2006).
14. D. H. E. Dubin, T. M. O'Neil, *Rev. Mod. Phys.* **71**, 87 (1999).
15. T. M. O'Neil, *Phys. Fluids* **23**, 2216 (1980).
16. J. R. Danielson, N. C. Hurst, C. M. Surko, "Progress Towards a Practical Multicell Positron Trap", AIP Conf. Proc. 1521, AIP Press, Melville NY, 2013, pp. 101–112.
17. N. C. Hurst, J. R. Danielson, C. J. Baker, C. M. Surko, *Phys. Rev. Lett.* **113**, 025004 (2014).
18. J. Fajans, E. Gilson, L. Friedland, *Phys. Rev. Lett.* **82**, 22 (1999).
19. C. J. Baker, N. C. Hurst, J. R. Danielson, C. M. Surko, "Electron plasma dynamics during autoresonant excitation of the diocotron mode", *Phys. Plasmas*, accepted (2015).
20. J. R. Danielson et. al. (unpublished).
21. C. A. Kapetanakos, A. W. Trivelpiece, *J. Appl. Phys.* **42**, 4841 (1971).
22. K. S. Fine, *Phys. Fluids B* **4**, 12 (1992).
23. N. R. Corngold, *Phys. Plasmas* **3**, 9 (1996).
24. K. S. Fine, C. F. Driscoll, *Phys. Plasmas* **5**, 3 (1998).